Materials Advances

ROYAL SOCIETY OF CHEMISTRY

PAPER

View Article Online
View Journal | View Issue

Cite this: *Mater. Adv.*, 2025, 6, 9104

The impact of growth method on the structural and electronic properties of Nb:Bi_2WO_6 thin films for high-power pn junction applications

Ichiro Takakuwa,[ab] Ryusuke Seino,[ab] Seiya Suzuki,[b] Keishi Nishio,[b] Shutaro Asanuma,[c] Yoshihiro Nemoto,[d] Yuki Nishimiya,[d] Yoichi Higashi,[e] Toshimitsu Ito[e] and Makoto Minohara *[a]

Received 29th August 2025,
Accepted 14th October 2025

DOI: 10.1039/d5ma00975h

rsc.li/materials-advances

Development of high-breakdown voltage power devices requires designing suitable p-type wide-bandgap oxide semiconductors. We investigated the growth of Nb-doped Bi_2WO_6 (Nb:BWO) thin films, which are promising candidates for p-type wide-bandgap oxide semiconductors, *via* pulsed laser deposition (PLD) and solid-phase epitaxy (SPE). While X-ray diffraction analyses confirmed the successful growth of the target Nb:BWO phase by both methods, X-ray fluorescence and photoemission spectroscopy revealed the presence of a significant Bi deficiency and defect states near the Fermi level in the PLD-grown film, in contrast to the SPE-grown film. These defects likely degrade device performance, as demonstrated by the poorer rectifying behavior of the Nb:BWO/β-Ga_2O_3 heterojunctions fabricated using the PLD-grown film. By contrast, the SPE-grown film showed better stoichiometry and improved electronic properties. These results indicate that SPE is a superior method for growing high-quality p-type oxide films suitable for power device applications.

Introduction

The increasing demand for energy-efficient and high-performance power conversion drives the development of advanced electrical systems in application such as electric mobility, next-generation communication networks, and the Internet of Things.[1–3] In this context, power devices play a crucial role in converting and controlling the usage of electrical energy with minimal loss.[3–6] However, silicon (Si)-based power devices are now approaching the intrinsic physical limits of the Si material, making it difficult to meet the requirements of emerging high-power applications,[7–9] motivating an intense research effort focused on the development of wide-bandgap (WBG) semiconductors such as silicon carbide (SiC), gallium nitride (GaN), and gallium oxide (Ga_2O_3) that are suitable for high-power applications.[10–12] In particular, β-Ga_2O_3, which is a representative oxide-based WBG semiconductor, has attracted strong interest due to its exceptionally high breakdown electric field of ~8 MV cm^{-1} and Baliga's figure of merit exceeding 3000, nearly ten times higher than that of SiC.[13] These advantages enable β-Ga_2O_3 to achieve both a higher breakdown voltage and lower on-resistance than SiC or GaN, making it a promising candidate material for use in next-generation power devices. However, the development of p-type β-Ga_2O_3 faces significant challenges. Previous studies have reported that even with acceptor doping, the acceptor levels are too deep and the hole mobility is intrinsically low.[8,14–16] These limitations hinder the realization of homojunction devices composed solely of β-Ga_2O_3, necessitating the use of external p-type semiconductors to form heterojunction structures. Unfortunately, the formation of interfacial reaction layers during the fabrication of such heterojunctions can degrade device performance.[17] To mitigate this issue, it is preferable to form junctions between oxide semiconductors, whose similar bonding configurations and chemical stability help suppress interfacial reactions.[18–21] Therefore, it is essential to explore p-type oxide semiconductors that are suitable for use in β-Ga_2O_3-based heterojunction devices.

Several studies have investigated heterojunction devices composed of β-Ga_2O_3 and conventional p-type oxide semiconductors such as NiO, Cu_2O, and SnO in an effort to achieve rectifying behaviour.[21–23] While NiO and Cu_2O possess relatively large bandgaps, their low dielectric constants can lead to premature breakdown on the p-side under high reverse bias conditions.[24] On the other hand, SnO offers a relatively high

[a] *Global Research and Development Centre for Business by Quantum-AI technology (G-QuAT), National Institute of Advanced Industrial Science and Technology (AIST), Tsukuba, 305-8568, Japan. E-mail: m-minohara@aist.go.jp*
[b] *Department of Materials Science and Technology, Tokyo University of Science, Katsushika, Tokyo, 125-8585, Japan*
[c] *Semiconductor Frontier Research Centre, AIST, Tsukuba, 305-8568, Japan*
[d] *Electron Microscopy Unit, National Institute for Materials Science (NIMS), Tsukuba, Ibaraki, 305-0047, Japan*
[e] *Department of Electronics and Manufacturing Core Electronics Technology Research Institute, AIST, Tsukuba, 305-8568, Japan*

dielectric constant, but its bandgap is not wide enough to support high-voltage operation.[25] Therefore, there is a crucial need to identify alternative p-type oxide semiconductors that simultaneously offer a sufficiently large bandgap and a high dielectric constant to achieve stable performance in high-voltage device applications. These characteristics are particularly important for high-voltage applications in fields such as electric mobility and energy infrastructure.

In the search for p-type oxide semiconductors with both large bandgaps and high dielectric constants, Bi_2WO_6 (BWO), a member of the Aurivillius-type oxide family, has emerged as a promising candidate material. Its two-dimensional layered structure, which is composed of alternating Bi_2O_3 layers and corner-sharing WO_6 octahedra, offers favourable electronic characteristics.[26,27] In particular, the valence band maximum (VBM) of BWO originates from the hybridization between Bi 6s and O 2p orbitals, which mitigates hole localization and enhances valence band dispersion.[28,29] To date, p-type conductivity and control of carrier density have been demonstrated for bulk polycrystalline BWO through acceptor doping with pentavalent ions such as Nb^{5+} and Ta^{5+}.[30] However, for practical device applications, it is essential to develop high-quality BWO thin films under precisely controlled growth conditions. While pulsed laser deposition (PLD), a non-equilibrium process, has been widely employed for the fabrication of BWO thin films, it often encounters challenges such as oxygen deficiency induced by the substrate and Bi volatilization under low oxygen partial pressure, both of which lead to compositional instability.[31–33] Meanwhile, previous studies on bulk polycrystalline BWO have demonstrated that Bi-defect-free materials can be synthesized *via* high-temperature sintering under atmospheric pressure.[30] Building on this insight, we devised a fabrication method in which a stoichiometric amorphous BWO film is first deposited by PLD, followed by crystallization through post-deposition annealing in air. This approach, which is based on solid-phase epitaxy (SPE), is expected to suppress off-stoichiometry and enable the formation of epitaxial films with improved compositional uniformity.

In this study, we investigated the fabrication of BWO thin films using PLD and SPE, and systematically evaluated their structural, compositional, and defect-related characteristics. To assess the impact of film quality on device performance, electrical measurements were performed for Nb:BWO/β-Ga_2O_3 heterojunction diodes. We found that SPE-grown BWO films exhibited superior crystallinity and stoichiometric control, resulting in improved rectifying behaviour of the heterojunction devices. These findings highlight the critical importance of the growth method selection for achieving high-quality p-type oxide thin films for power device applications.

Experimental

Materials and methods

Nb(10 at%)-doped BWO films with a thickness of 200 nm were grown on (001)-oriented Nb-doped $SrTiO_3$ (Nb:STO) or (010)-oriented Si(0.0052 wt%)-doped β-Ga_2O_3 substrates. Thin films were deposited using a sintered Nb:BWO target (Kojundo Chemical Laboratory Co., Ltd). A Nd-doped yttrium aluminum garnet laser was used for ablation in its frequency-quadrupled mode (λ = 266 nm) at a repetition rate of 5 Hz. Prior to film deposition, the Nb:STO and β-Ga_2O_3 substrates were annealed at 850 and 900 °C, respectively, in an electric tube furnace (KOYO Thermo System). For the PLD process, the substrates were maintained at 600 °C under a partial oxygen pressure (P_{O_2}) of 4.0 Pa. In another growth process, the films were deposited at room temperature under P_{O_2} = 7.0 Pa by laser ablation. After deposition, the Nb:BWO films were crystalized on both Nb:STO and β-Ga_2O_3 substrates by post-annealing at 700 °C for 1 h in air at atmospheric pressure in the tube furnace. It should be noted that the Nb:BWO film grown on the Nb:STO substrate was epitaxially aligned along three crystallographic axes (see details in the Results and discussion section), whereas the film on the β-Ga_2O_3 substrate was randomly oriented.

Characterization

X-ray diffraction (XRD) measurements were performed using a Rigaku SmartLab diffractometer (Rigaku Corp.) operated in the parallel-beam mode with a Cu Kα_1 radiation source (λ = 1.54056 Å) at 45 kV and 200 mA. The chemical composition of Nb:BWO films was analysed by X-ray fluorescence (XRF) measurements using a ZSX Primus II spectrometer (Rigaku Corp.). The crystallographic arrangement around the interface between Nb:BWO and Nb:STO was investigated using high-angle annular dark field scanning transmission electron microscopy (HAADF-STEM) measurements. Photoelectron spectroscopy (PES) measurements were carried out at room temperature using a VG-Scienta SES-200 analyser at the undulator beamline BL-13B of the Photon Factory, KEK.[34]

Device fabrication

Electrodes were patterned using the maskless lithography technique. To obtain ohmic contact with both Nb:BWO and β-Ga_2O_3 layers, a 10-nm-thick Ti layer was deposited by sputtering, followed by the deposition of a 90-nm-thick Au layer. The electrode diameter was 100 μm. Current density–voltage (J–V) measurement was conducted for 70 diodes at room temperature under ambient pressure using a probe connected to a Keysight B1500A semiconductor parameter analyser. During all measurements, the bottom electrode on the β-Ga_2O_3 side was grounded, while voltage bias was applied to the top electrode.

Density functional theory (DFT) calculations

The electronic structure of Bi_2WO_6 (BWO) was calculated using the Quantum ESPRESSO simulation package,[35,36] applying the plane-wave pseudopotential method within the density functional theory (DFT) framework. The Perdew–Burke–Ernzerhof (PBE) form of the generalized gradient approximation (GGA) was employed for the exchange–correlation functional. The ionic core potential was approximated using the projector-augmented wave pseudopotentials[37,38] with the valence electron orbitals Bi(6s/6p/5d), W(5s/6s/5p/6p/5d), and O(2s/2p). An orthorhombic crystal structure (space group $Pca2_1$, #29) was adopted with fixed lattice parameters: a = 10.302 Bohr, b/a = 3.0183, and c/a = 1.0000. The kinetic energy cutoff for the plane-

wave basis set was set to 50 Ry (680 eV), and the self-consistent field (SCF) calculations were converged to a threshold of 1.0×10^{-8} Ry in the total energy. For Brillouin zone integration, an unshifted $(6 \times 2 \times 6)$ Monkhorst–Pack k-point mesh was used for SCF calculations, and a denser $(12 \times 4 \times 12)$ grid was applied for the projected density of states (PDOS) calculations.

Results and discussion

Structural, microstructural, and compositional characterization

Fig. 1a shows the XRD 2θ-ω patterns of the Nb:BWO films grown by PLD and SPE. For the PLD sample, the intensities of the (020), (060) and (0120) Bragg peaks are noticeably lower compared to those of the SPE sample. In addition, several impurity peaks are observed at approximately 23.1°, 47.1° and 73.6°. Furthermore, the Bi/W ratio evaluated from the XRF measurements was approximately 0.2, suggesting that significant Bi desorption occurred above the temperature range of 300–400 °C during PLD growth (Fig. 1b). Therefore, the impurity peaks observed in the XRD measurements can be attributed to residual tungsten compounds, such as WO_3. While the Bi/W ratio maintained close to the nominal value at the growth temperature below 300 °C, no $(0k0)$ Bragg peaks were detected, suggesting that such temperatures are insufficient to induce crystallization of the Nb:BWO precursors during the deposition process. Such a severe deviation from stoichiometry, and particularly the significant Bi deficiency, can degrade the electronic properties of the film by introducing charge compensation defects and disrupting the conduction pathways. In turn, this compositional imbalance is expected to adversely affect the rectifying behaviour and carrier transport in the heterojunction device.

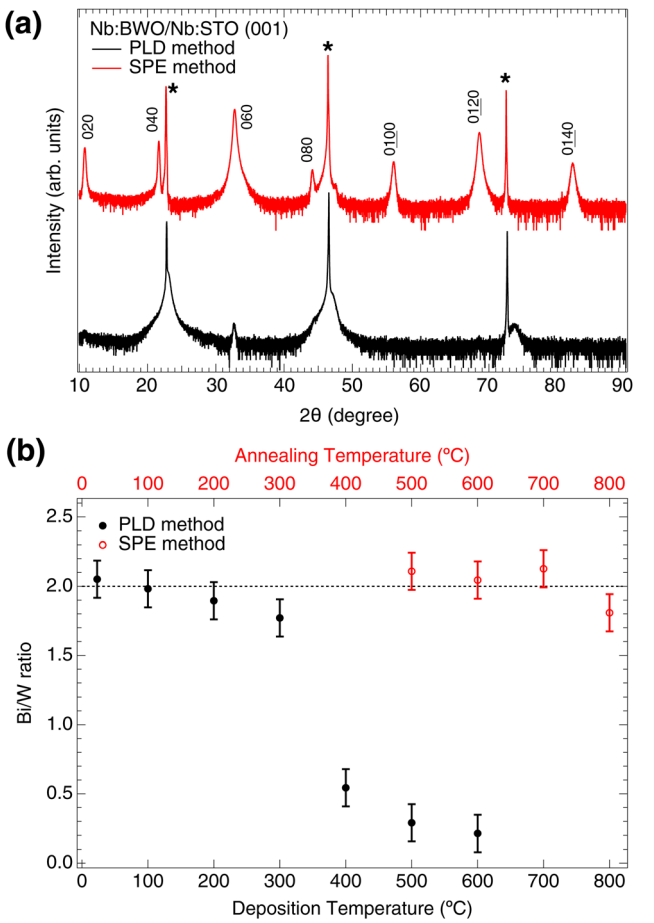

Fig. 1 (a) XRD 2θ-ω scan of Nb:BWO thin films prepared on Nb:STO by PLD and SPE methods. (b) Bi/W composition ratio in Nb:BWO thin films analysed by XRF.

By contrast, well-defined $(0k0)$ Bragg peaks, which are characteristic of the ideal Bi_2WO_6 structure, without any impurity peaks are clearly observed for the SPE-grown Nb:BWO film (Fig. 1a). The Bi/W ratio of the SPE-grown film was close to 2 (Fig. 1b), indicating that Bi desorption did not occur during the SPE process, even though the annealing temperature was higher than the deposition temperature used in PLD growth. Taking into account the previous reports on the successful growth of BWO films by the PLD method under oxygen pressures higher than those used in our study, the high oxygen partial pressure (P_{O_2}) during atmospheric annealing in the SPE process likely suppresses Bi volatilization by shifting the thermodynamic equilibrium toward the formation of Bi–O bonds.[39,40] This shifts the vapor pressure of Bi-containing species such as Bi_2O_3 to lower values, thereby preventing Bi loss.

Fig. 2 shows the reciprocal space map (RSM) around the Nb:STO (113) reflection for the SPE-grown film. The (2012) reflection of the Nb:BWO film is clearly observed, although it is slightly offset along the in-plane axis from the Nb:STO (113) Bragg peak. This lateral shift suggests partial relaxation of the in-plane tensile strain, which originates from the lattice mismatch between Nb:BWO and Nb:STO. Based on Q_x and Q_y positions of the Nb:BWO (2120) reflection, the in-plane and out-of-plane lattice constants are estimated to be 0.5461 ± 0.023 nm and 1.6404 ± 0.002 nm, respectively. Considering that the bulk lattice constants of Nb:BWO are 0.5437 nm (in-plane) and 1.6430 nm (out-of-plane),[30] the tensile strain is only partially accommodated in the film.

Fig. 3a and b show the pole figures of the (2120) reflection of the SPE-grown Nb:BWO film and the (113) reflection of the Nb:STO substrate, respectively. Distinct peaks appear every 90° for both the film and substrate, indicating fourfold symmetry. Notably, the peak positions of the Nb:BWO film are rotated by 45° relative to those of the Nb:STO substrate. This angular offset indicates that the Nb:BWO film is epitaxially grown with a 45° in-plane rotation relative to the underlying Nb:STO substrate. Such a rotational relationship implies that the [100] axis of Nb:BWO is aligned along the [110] direction of Nb:STO, a configuration commonly observed in epitaxial growth involving lattice-mismatch. The appearance of this configuration is driven by the need to minimise the interfacial energy. Fig. 2c shows the HAADF-STEM image of the Nb:BWO/Nb:STO interface observed along the [100] direction of the Nb:STO substrate. Periodic arrays of Sr (green spheres in the

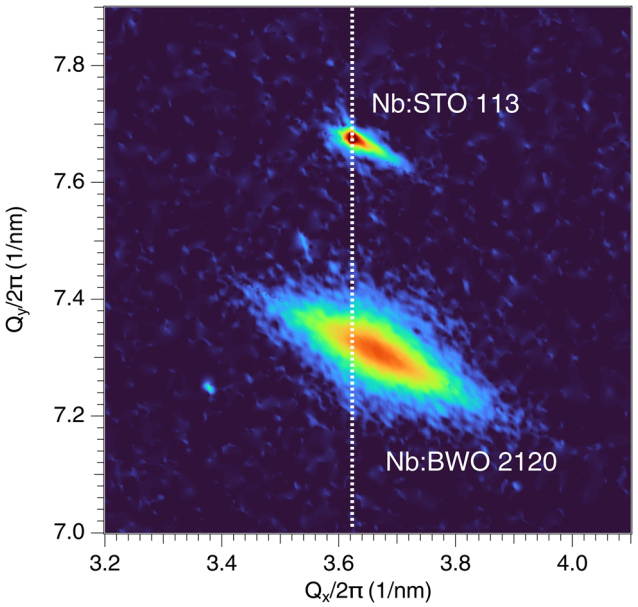

Fig. 2 RSM around the Nb:STO (113) Bragg peak of the SPE sample.

schematic insets) and Ti (blue spheres) atoms in the Nb:STO substrate, as well as Bi (purple spheres) and W (grey spheres) atoms in the Nb:BWO film, are clearly observed and exhibit an epitaxial relationship. Notably, this periodic structure corresponds to a projection along the [100] direction for the Nb:STO substrate and along the [110] direction for the Nb:BWO film, consistent with the findings from the pole figure analysis. The epitaxial relationship observed in this work is in good agreement with previous reports.[41–43]

With the crystal structure and epitaxial relationship clearly established, we next examine the homogeneity along the depth direction of the Nb:BWO film grown by the SPE method. To assess structural uniformity, high-resolution TEM observations were performed from the Nb:BWO/Nb:STO interface to the film surface. Fig. 4a shows the high-resolution TEM images of the SPE-grown Nb:BWO film. The characteristic periodic structure of the layered phase of Nb:BWO is clearly preserved from the interface to the surface. Moreover, no structural defects such as dislocations, stacking faults, or grain boundaries were detected within the observed area, indicating high uniformity throughout the film. These features were consistently observed across multiple regions of the film, confirming that the observed structural uniformity is representative of the overall film quality.

Fig. 4b shows the depth profiles of the Bi, W, and O ions in the Nb:BWO film grown on the Nb:STO substrate, obtained through the SIMS measurement. Except for the anomalous intensity variations near the surface due to matrix effects,[44,45] the intensities of the Bi, W, and O ions are found to be nearly uniform throughout the film. Furthermore, no detectable signals of Bi and W are observed in the substrate region, indicating the absence of appreciable interdiffusion of these elements into the substrate. The oxygen signal in the substrate is roughly half of that in the film, consistent with the expected compositional difference between the film and the substrate.

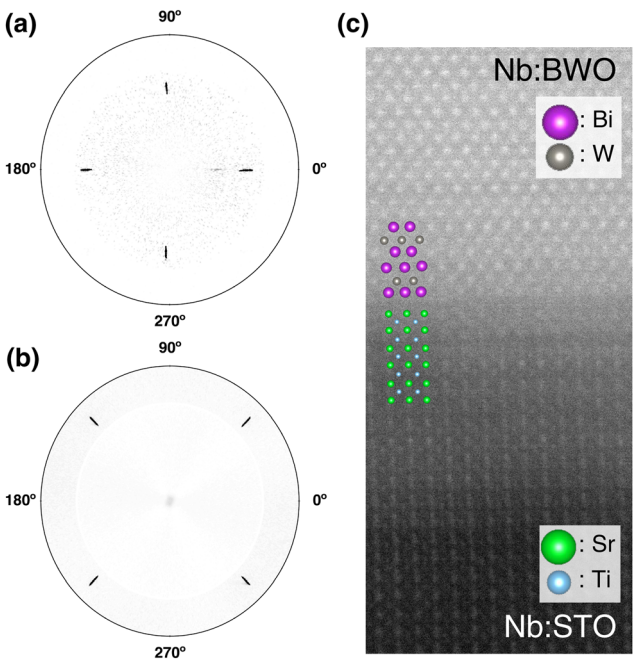

Fig. 3 Pole figures of (a) the (2120) plane of the SPE-grown Nb:BWO film, and (b) the (113) plane of the Nb:STO substrate. (c) HAADF-STEM image of the Nb:BWO/Nb:STO interface of the SPE sample.

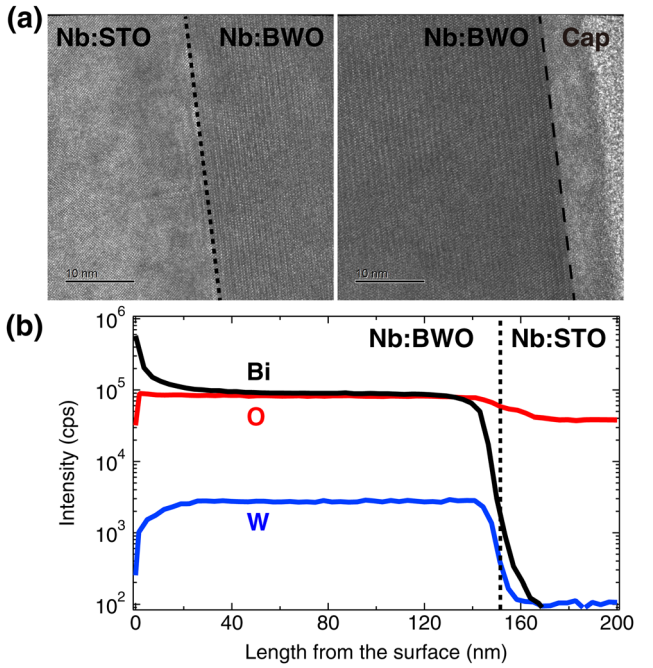

Fig. 4 (a) High-resolution TEM images of the Nb:BWO/Nb:STO interface and Nb:BWO/Cap layer interface in the SPE sample. (b) Depth profiles of Bi, W, and O in the SPE sample obtained by SIMS analysis.

Electronic structure analysis

Fig. 5a and b show the Bi 4f and W 4f core-level photoemission spectra of the Nb:BWO films, respectively. In contrast to the PLD-grown films, which exhibit clear shoulder features in both the Bi 4f and W 4f spectra, the SPE-grown films show no such features, and the spectra can be fitted well assuming a single chemical component, indicating the absence of chemical inhomogeneity. The shoulder features observed in the Bi 4f and W 4f spectra of the PLD-grown films are likely due to the presence of chemically distinct species, such as sub-stoichiometric phases or lower oxidation states (*e.g.*, Bi^0 or W^{5+}), which may form due to off-stoichiometry. For the W 4f spectrum of the PLD-grown film, not only are shoulder components present, but the fitted peaks themselves show noticeable broadening compared to those of the SPE-grown film. This spectral broadening suggests the coexistence of multiple W chemical environments, possibly arising from the presence of non-stoichiometric secondary phases including WO_3 impurities[46–48] found in XRD measurements. These observations further support the presence of chemical inhomogeneity in the PLD-grown film.

Fig. 5c shows the valence band (VB) photoemission spectra and O *K*-edge X-ray absorption spectra (XAS) of Nb:BWO films grown by PLD and SPE, along with the calculated PDOS of the VB and the conduction band shown in Fig. 5d. The measured spectrum for the SPE-grown film exhibits good agreement with the calculated DOS, indicating that the electronic structure near the VBM is reproduced well by the theoretical model. By contrast, a distinct electronic state is observed at the Fermi level (E_F) in the PLD-grown film, suggesting the presence of defect-induced states or unintentional doping. Comparison with the calculated DOS shows that Bi-related states such as peaks *e* and *f* are absent in the PES spectrum of the PLD-grown sample. Moreover, the O 2p and Bi 6p hybridization state is quite weak in the VB spectrum of the PLD-grown film. This observation is consistent with the XRF results, which indicate a Bi deficiency (V_{Bi}) in the film, induced by thermally driven oxygen desorption during PLD growth, suggesting the formation of donor-like states associated with V_{Bi}.[49] These states likely contribute to the observed intensity at E_F.

It is important to note that the SPE-grown film exhibits a clear upward shift of the VBM compared to the PLD-grown film. This shift suggests a reduced electron concentration due to suppression of V_{Bi} formation. However, the magnitude of the VBM shift is limited, suggesting only a partial reduction in donor-like defects. This limited shift may be attributed to the presence of oxygen vacancies, which act as compensating donors and hinder effective hole doping. Taken together, these results indicate that complete suppression of donor-type defects has not yet been achieved, even in the SPE-grown film under the current conditions. Addressing these residual donor states will be an important challenge for further optimization of the material in future studies. Furthermore, taken together, the VB and XAS spectra suggest a slight variation in the bandgap of the grown Nb:BWO films. Notably, the bandgap of the SPE-grown film appears to be closer to the reported bulk value than that of the PLD-grown counterpart.[27] Although this

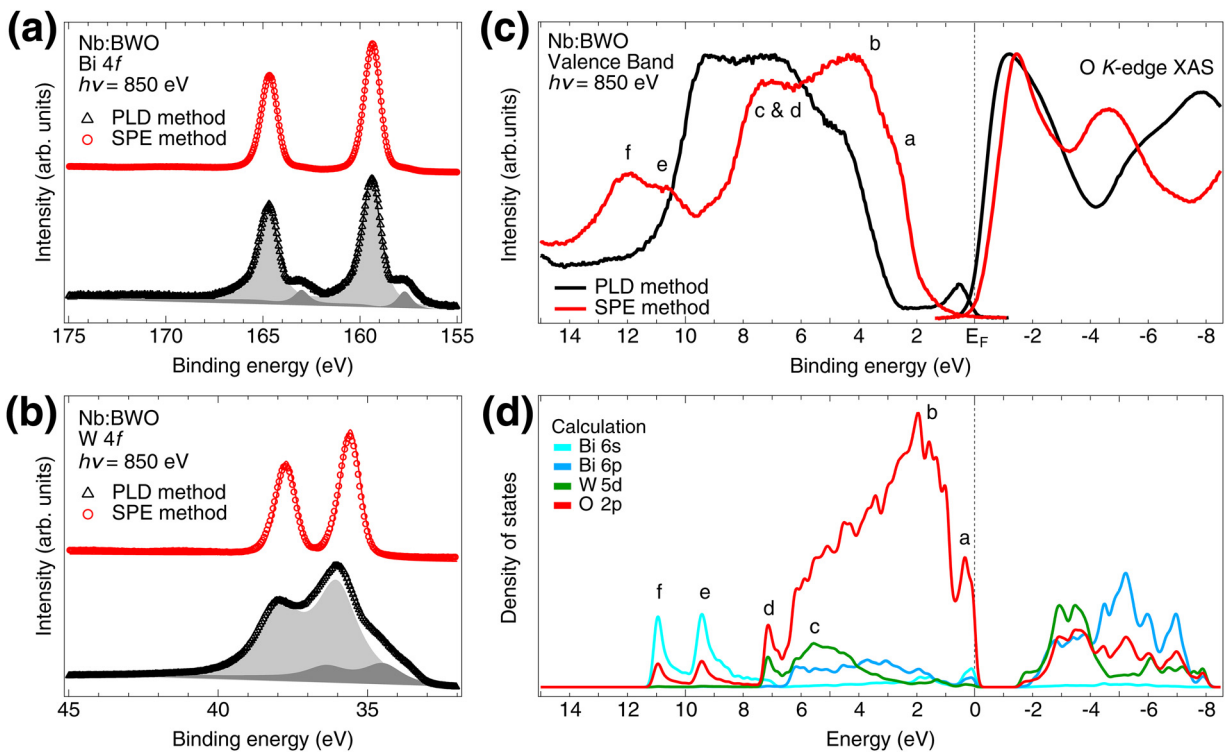

Fig. 5 (a) Bi 4f and (b) W 4f core-level spectra of PLD and SPE samples. (c) Valence band PES and O K-edge XAS spectra of PLD and SPE samples. (d) DOS of Bi_2WO_6 from DFT simulations.

observation is not conclusive, as it may be influenced by spectral broadening and defect-induced effects, this difference in the band gap values may reflect subtle variations in defect concentration or local structural disorder, particularly in the PLD-grown film examined in this study.

The combined results of structural characterization and spectroscopic analyses indicate that the PLD-grown film significantly deviates from stoichiometry, leading to the formation of defect states within the bandgap. By contrast, the SPE-grown film exhibits a nearly ideal stoichiometric composition, with negligible in-gap states. This fundamental difference is expected to have a significant impact on the device performance of power diodes employing Nb:BWO as the p-type layer in combination with β-Ga_2O_3.

Preliminary demonstration of a pn heterojunction diode

Given the substantial improvements in crystalline quality, stoichiometry, and electronic states achieved by the SPE method, its impact on the electrical characteristics of the power diodes was evaluated. Fig. 6 presents the representative current density–voltage (J–V) characteristics of the Nb:BWO/β-Ga_2O_3 heterojunction diodes fabricated to examine the impact of film quality on device performance. During the measurements, the β-Ga_2O_3 side was grounded, while voltage bias was applied to the Nb:BWO side. While both diodes exhibited rectifying behaviour, their characteristics differ significantly. The current density in the forward-bias region of the PLD-grown diode is more than one order of magnitude lower than that of its SPE-grown counterpart. Moreover, the PLD-grown diode exhibits a reverse leakage current on the order of 10^{-6} A cm^{-2}, which is significantly higher than that of the SPE-grown diode. Consequently, the ON/OFF current ratio was enhanced from approximately one or two orders of magnitude for PLD-grown diodes to the mid-five orders of magnitude for SPE-grown ones, with a standard deviation of about 10–20% among different devices.

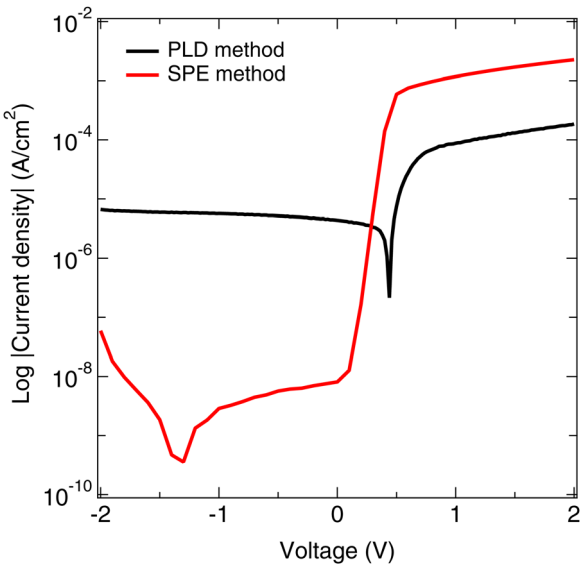

Fig. 6 J–V characteristics of Nb:BWO/β-Ga_2O_3 pn junction diodes using Nb:BWO thin films prepared by PLD and SPE methods.

It is well-known that the J–V characteristics of a heterojunction in the forward-bias region can be described using the Shockley diode equation:[50]

$$J = J_s\left[\exp\left(\frac{qV}{\eta k_B T}\right) - 1\right], \quad (1)$$

where q is the electron charge, T is the absolute temperature, k_B is the Boltzmann constant (1.381×10^{-23} JK^{-1}), J_s is the reverse saturation current, V is the applied voltage, and η is the ideality factor. The values of η for the PLD-grown diode and the SPE-grown diode were found to be 2.58 ± 0.06 and 1.16 ± 0.06, respectively. Furthermore, the effective barrier height ($\Phi_{B,eff}$) was estimated using the Richardson–Dushman equation:[51]

$$\Phi_{B,eff} = \frac{k_B T}{q}\ln\left(\frac{A^* T^2}{J_s}\right) \quad (2)$$

where A^* is the Richardson–Dushman constant, which is equal to 33.65 A K^{-2} cm^{-2} for β-Ga_2O_3.[52,53] The $\Phi_{B,eff}$ values were estimated to be 0.71 eV for the PLD-grown diode and 1.10 eV for the SPE-grown diode. Considering that the reported work functions of BWO and β-Ga_2O_3 differ by approximately 1.0 eV,[54,55] the SPE-grown diode forms a nearly ideal junction, in contrast to the PLD-grown diode, which deviates from ideality. The reduced $\Phi_{B,eff}$ and η observed in the PLD-grown diode are consistent with the presence of non-ideal interface properties, such as defect states. Such defect states induced by Bi deficiency may lead to Fermi level pinning and degrade the diode characteristics. This results in an increased turn-on voltage and reduced forward current in the PLD-grown diode, consistent with the observed electrical characteristics. By contrast, the SPE-grown diode, for which Bi deficiency is effectively suppressed, shows a lower turn-on voltage and higher forward current, consistent with minimal Fermi level pinning due to the improved interface quality. Under reverse bias, the SPE-grown diode exhibits a markedly reduced leakage current. This improvement is attributed to the alleviation of Fermi level pinning, as evidenced by the results of the PES measurements shown in Fig. 5c, which indicates an upward shift of both the VBM and the conduction band minimum. Consequently, the conduction band offset increases, leading to a more effective suppression of carrier injections under reverse bias. As the applied voltage reaches −1.5 V, a noticeable increase in current density is observed. Based on the extracted $\Phi_{B,eff}$, dopant concentrations, and dielectric constants of Nb:BWO and β-Ga_2O_3,[13,27] the electric field at the heterointerface is estimated to be approximately 4.5 MV cm^{-1}. Although this value is smaller than the critical electric field of β-Ga_2O_3 (7 MV cm^{-1}),[13] it is sufficiently close to be regarded as qualitatively reasonable, especially given that the preliminary diode demonstrated does not incorporate a mesa structure, and potential edge effects may influence the breakdown behaviour. This consistency further supports the reasonableness of the observed J–V characteristics. Taken together, these results indicate that the Nb:BWO/β-Ga_2O_3 heterojunction fabricated *via* the SPE method exhibits close-to-ideal interfacial behaviour under both forward and reverse bias conditions.

These findings highlight the significant role of cation stoichiometry and particularly Bi deficiency in determining the interfacial electronic structure and rectifying the performance of complex oxide heterojunctions. Our results underscore the importance of precise chemical control of the interface for realizing high-performance oxide-based devices. Moreover, the rectifying characteristics typical of a p–n diode are not observed in the BWO/Ga_2O_3 heterojunction fabricated *via* hydrothermal synthesis.[56] This phenomenon is likely due to the substantial generation of free electrons in BWO, presumably induced by oxygen vacancies formed during the deposition process, which render the material effectively n-type. Therefore, selecting deposition techniques that suppress oxygen vacancy formation during growth could also be an important factor for improving the diode characteristics.

Conclusions

In summary, Nb-doped Bi_2WO_6 (Nb:BWO) thin films were fabricated by pulsed laser deposition and solid-phase epitaxy, and their structural, electronic, and electrical properties were systematically investigated. The SPE films exhibited superior crystallinity and stoichiometry, whereas the PLD films showed significant Bi deficiency and associated defect states. These structural differences were reflected in the electrical properties: SPE films enabled better rectifying behaviour in heterojunction diodes due to the absence of defect-related recombination paths, while PLD films suffered from degraded performance owing to the presence of Bi vacancies. These findings highlight the crucial role of defect suppression and stoichiometry control for realizing p-type oxide semiconductors with low leakage current and high on/off ratios required for power device applications. The SPE method was demonstrated to be a promising approach for the fabrication of high-quality Nb:BWO thin films for use in next-generation wide-bandgap power electronics. This study shows that selecting an appropriate growth method is essential for improving the electronic properties of high-power diodes, particularly in oxide semiconductors containing volatile elements, providing insights directly relevant to deposition process development.

Author contributions

M. M. and K. N. designed the experiments. I. T. and S. S. synthesized the films. I. T., R. S., and S. A. fabricated the p–n diode. T. I. grew Ga_2O_3 single crystals. I. T., R. S., S. S., and M. M. performed PES measurements. Y. H. performed density functional theory calculations. Yu. N. fabricated the samples for TEM measurements, and Yo. N. performed TEM measurements. We would like to thank Editage (**https://www.editage.jp**) for English language editing and their assistance in creating the graphical abstract for this paper.

Conflicts of interest

There are no conflicts of interest to declare.

Data availability

The datasets generated and analyzed during the current study, including both experimental and simulation data, are available in the AIST repository at DOI: **https://doi.org/10.57765/2003400**.

Supplementary information (SI): Cross-sectional SEM image of the Nb:BWO film grown on the Nb:STO substrate (Fig. S1) and the XRD pattern of the Nb:BWO film grown on β-Ga_2O_3 (Fig. S2). See DOI: **https://doi.org/10.1039/d5ma00975h**.

Acknowledgements

We thank Dr K. Ozawa and Dr K. Mase for providing technical support for the beamline experiments. This work was supported by the Grant-in-Aid for Scientific Research (No. 24K08254) from the Japan Society for the Promotion of Science (JSPS). The work at KEK-PF was performed with the approval of the Program Advisory Committee (Proposals No. 2021S2-003 and 2023G507) at the Institute of Materials Structure Science, KEK. A part of this work was supported by ARIM of MEXT (JPMXP1224NM0220).

Notes and references

1 S. Granata, P. Zanchetta, M. D. Benedetto, C. Terlizzi, R. Leuzzi and S. Bifaretti, Power Electronics Converters for the Internet of Energy: A Review, *Energies*, 2022, **15**, 2604.
2 J. L. Afonso, L. A. L. Cardoso, D. Pedrosa, T. J. C. Sousa, L. Machado, M. Tanta and V. Monteiro, A Review on Power Electronics Technologies for Electric Mobility, *Energies*, 2020, **13**, 6343.
3 S. Mao, T. Wu, X. Lu, J. Popovic and J. A. Ferreira, 6th Electron. Syst.-Integr. Technol. Conf. (ESTC), 2016, pp. 1–5.
4 J. L. Afonso, M. Tanta, J. G. O. Pinto, L. F. C. Monteiro, L. Machado, T. J. C. Sousa and V. Monteiro, A Review on Power Electronics Technologies for Power Quality Improvement, *Energies*, 2021, **14**, 8585.
5 M. Luna, High-Efficiency and High-Performance Power Electronics for Power Grids and Electrical Drives, *Energies*, 2022, **15**, 5844.
6 Y. Wang, O. Lucia, Z. Zhang, Y. Guan and D. Xu, Review of very high frequency power converters and related technologies, *IET Power Electron.*, 2020, **13**, 1711.
7 Z. Chen and A. Q. Huang, Extreme high efficiency enabled by silicon carbide (SiC) power devices, *Mater. Sci. Semicond. Process.*, 2024, **172**, 108052.
8 F. Iacopi, M. Van Hove, M. Charles and K. Endo, Power electronics with wide bandgap materials: Toward greener, more efficient technologies, *MRS Bull.*, 2015, **40**, 390.
9 O. S. Chaudhary, M. Denai, S. S. Refaat and G. Pissanidis, Technology and Applications of Wide Bandgap Semiconductor Materials: Current State and Future Trends, *Energies*, 2023, **16**, 6689.
10 X. Chen, F. Li and H. L. Hess, Trench gate β-Ga_2O_3 MOSFETs: a review, *Eng. Res. Express*, 2023, **5**, 012004.

11 Y. He, F. Zhao, B. Huang, T. Zhang and H. Zhu, A Review of β-Ga_2O_3 Power Diodes, *Mater.*, 2024, **17**, 1870.
12 S. Sun, C. Wang, S. Alghamdi, H. Zhou, Y. Hao and J. Zhang, Recent Advanced Ultra-Wide Bandgap β-Ga_2O_3 Material and Device Technologies, *Adv. Electron. Mater.*, 2024, **11**, 2300844.
13 M. Higashiwaki, β-Ga_2O_3 material properties, growth technologies, and devices: a review, *AAPPS Bull.*, 2022, **32**, 3.
14 M. J. Tadjer, J. L. Lyons, N. Nepal, J. A. Freitas Jr., A. D. Koehler and G. M. Foster, Review—Theory and characterization of doping and defects in β-Ga_2O_3, *ECS J. Solid State Sci. Technol.*, 2019, **8**, Q3187.
15 M. D. McCluskey, Point defects in Ga_2O_3, *J. Appl. Phys.*, 2020, **127**, 101101.
16 K. Kaneko, S. Takemoto, S. Kan, T. Shinohe and S. Fujita, P-type semiconductors in gallium oxide electronics, CS MANTECH 2019 - 2019 International Conference on Compound Semiconductor Manufacturing Technology, Digest of Papers, 2019.
17 J. T. Gibbon, L. Jones, J. W. Roberts, M. Althobaiti, P. R. Chalker, I. Z. Mitrovic and V. R. Dhanak, Band alignments at Ga_2O_3 heterojunction interfaces with Si and Ge, *AIP Adv.*, 2018, **8**, 065011.
18 C. V. Prasad, J. H. Park, J. Y. Min, W. Song, M. Labed, Y. Jung, S. Kyoung, S. Kim, N. Sengouga and Y. S. Rim, Interface engineering of p-type quaternary metal oxide semiconductor interlayer-embedded β-Ga_2O_3 Schottky barrier diode, *Mater. Today Phys.*, 2023, **30**, 100932.
19 Z. Liang, M. Su, Y. Zhou, L. Gong, C. Zhao, K. Chen, F. Xie, W. Zhang, J. Chen, P. Liu and W. Xie, Interaction at the silicon/transition metal oxide heterojunction interface and its effect on the photovoltaic performance, *Phys. Chem. Chem. Phys.*, 2015, **17**, 27409.
20 S. Ghosh, M. Baral, R. Kamparath, R. J. Choudhary, D. M. Phase, S. D. Singh and T. Ganguli, Epitaxial growth and interface band alignment studies of all oxide α-Cr_2O_3/β-Ga_2O_3 p-n heterojunction, *Appl. Phys. Lett.*, 2019, **115**, 061602.
21 K. Tetzner, K. Egbo, M. Klupsch, R.-S. Unger, A. Popp, T.-S. Chou, S. B. Anoos, Z. Galazka, A. Trampert, O. Bierwagen and J. Würfl, SnO/β-Ga_2O_3 heterojunction field-effect transistors and vertical p–n diodes, *Appl. Phys. Lett.*, 2022, **120**, 112110.
22 Y. Liu, S. M. W. Witsell, J. F. Conley and S. Krishnamoorthy, *arXiv*, 2025, preprint, arXiv:2503.17895, DOI: **10.48550/arXiv.2503.17895**.
23 Y. Jia, S. Sato, A. Traoré, R. Morita, E. Broccoli, F. F. Florena, M. M. Islam, H. Okumura and T. Sakurai, Electrical properties of vertical Cu_2O/β-Ga_2O_3 (001) p–n diodes, *AIP Adv.*, 2023, **13**, 105306.
24 M. Mehta and S. Avasthi, The possibility of gallium oxide (β-Ga_2O_3) heterojunction bipolar transistors, *Phys. Scr.*, 2023, **98**, 025013.
25 M. Budde, D. Splith, P. Mazzolini, A. Tahraoui, J. Feldl, M. Ramsteiner, H. von Wenckstern, M. Grundmann and O. Bierwagen, SnO/β-Ga_2O_3 vertical pn heterojunction diodes, *Appl. Phys. Lett.*, 2020, **117**, 252106.
26 K. S. Knight, The crystal structure of russellite; a re-determination using neutron powder diffraction of synthetic Bi_2WO_6, *Mineral. Mag.*, 1992, **56**, 399.
27 X. Liu, P. Long, Z. Sun and Z. Yi, Optical, electrical and photoelectric properties of layered-perovskite ferroelectric Bi_2WO_6 crystals, *J. Mater. Chem. C*, 2016, **4**, 7563.
28 X. Liu and H.-Q. Fan, Theoretical studies on electronic structure and optical properties of Bi_2WO_6, *Optik*, 2018, **158**, 962.
29 H. Ahmad, A. Rauf, A. Ahmad, A. Ulhaq and S. Muhammad, First-principles study on the electronic and optical properties of Bi_2WO_6, *RSC Adv.*, 2021, **11**, 32330.
30 M. Minohara, Y. Dobashi, N. Kikuchi, S. Suzuki, A. Samizo, T. Honda, K. Nishio and Y. Aiura, Control of Hole Density in Russellite Bi_2WO_6 *via* Intentional Chemical Doping, *Inorg. Chem.*, 2023, **62**, 8303.
31 S. Das, T. Ohkubo, S. Kasai and Y. Kozuka, Deterministic Influence of Substrate-Induced Oxygen Vacancy Diffusion on Bi_2WO_6 Thin Film Growth, *Cryst. Growth Des.*, 2021, **21**, 404.
32 S. Havelia, S. Wang, M. Skowronski and P. A. Salvador, Controlling the Bi content, phase formation, and epitaxial nature of $BiMnO_3$ thin films fabricated using conventional pulsed laser deposition, hybrid pulsed laser deposition, and solid state epitaxy, *J. Appl. Phys.*, 2009, **106**, 123509.
33 H. Shi, B. Zou, Z. Li, M. Luo and W. Wang, Direct observation of oxygen-vacancy formation and structural changes in Bi_2WO_6 nanoflakes induced by electron irradiation, *Beilstein J. Nanotechnol.*, 2019, **10**, 1434.
34 Y. Aiura, K. Ozawa, K. Mase, M. Minohara and S. Suzuki, Development of a high-precision XYZ translator and estimation of beam profile of the vacuum ultraviolet and soft X-ray undulator beamline BL-13B at the Photon Factory, *J. Synchrotron Radiat.*, 2020, **27**, 923.
35 P. Giannozzi, S. Baroni, N. Bonini, M. Calandra, R. Car, C. Cavazzoni, D. Ceresoli, G. L. Chiarotti, M. Cococcioni, I. Dabo, A. Dal Corso, S. de Gironcoli, S. Fabris, G. Fratesi, R. Gebauer, U. Gerstmann, C. Gougoussis, A. Kokalj, M. Lazzeri, L. Martin-Samos, N. Marzari, F. Mauri, R. Mazzarello, S. Paolini, A. Pasquarello, L. Paulatto, C. Sbraccia, S. Scandolo, G. Sclauzero, A. P. Seitsonen, A. Smogunov, P. Umari and R. M. Wentzcovitch, QUANTUM ESPRESSO: a modular and open-source software project for quantum simulations of materials, *J. Phys.: Condens. Matter*, 2009, **21**, 395502.
36 P. Giannozzi, O. Andreussi, T. Brumme, O. Bunau, M. Buongiorno Nardelli, M. Calandra, R. Car, C. Cavazzoni, D. Ceresoli, M. Cococcioni, N. Colonna, I. Carnimeo, A. Dal Corso, S. de Gironcoli, P. Delugas, R. A. DiStasio Jr, A. Ferretti, A. Floris, G. Fratesi, G. Fugallo, R. Gebauer, U. Gerstmann, F. Giustino, T. Gorni, J. Jia, M. Kawamura, H.-Y. Ko, A. Kokalj, E. Küçükbenli, M. Lazzeri, M. Marsili, N. Marzari, F. Mauri, N. L. Nguyen, H.-V. Nguyen, A. Otero-de-la-Roza, L. Paulatto, S. Poncé, D. Rocca, R. Sabatini, B. Santra, M. Schlipf, A. P. Seitsonen, A. Smogunov, I. Timrov,

T. Thonhauser, P. Umari, N. Vast, X. Wu and S. Baroni, Advanced capabilities for materials modelling with Quantum ESPRESSO, *J. Phys.: Condens. Matter*, 2017, **29**, 465901.
37 G. Kresse and D. Joubert, From ultrasoft pseudopotentials to the projector augmented-wave method, *Phys. Rev. B: Condens. Matter Mater. Phys.*, 1999, **59**, 1758.
38 A. Dal Corso, Pseudopotentials periodic table: From H to Pu, *Comput. Mater. Sci.*, 2014, **95**, 337.
39 D. Risold, B. Hallstedt, L. J. Gauckler, H. L. Lukas and S. G. Fries, The bismuth–oxygen system, *J. Phase Equilib.*, 1995, **16**, 223.
40 E. Oniyama and P. G. Wahlbeck, Phase equilibria in the bismuth–oxygen system, *J. Phys. Chem. B*, 1998, **102**, 4420.
41 K. Nishio, C. Kudo, T. Nagahama, T. Manabe, I. Yamaguchi, Y. Watanabe and T. Tsuchiya, Preparation and characterization of epitaxial Bi_2WO_6 thin films prepared by a sol–gel process, *MRS Proc.*, 2000, **623**, 377.
42 C. Wang, X. Ke, J. Wang, R. Liang, Z. Luo, Y. Tian, D. Yi, Q. Zhang, J. Wang, X.-F. Han, G. Van Tendeloo, L.-Q. Chen, C.-W. Nan, R. Ramesh and J. Zhang, Ferroelastic switching in a layered-perovskite thin film, *Nat. Commun.*, 2016, **7**, 10636.
43 J. Jeong, J. Mun, S. Das, J. Kim, J. R. Kim, W. Peng, M. Kim and T. W. Noh, Growth and Atomically Resolved Polarization Mapping of Ferroelectric Bi_2WO_6 Thin Films, *ACS Appl. Electron. Mater.*, 2021, **3**, 721.
44 M. P. Seah and A. G. Shard, The matrix effect in secondary ion mass spectrometry, *Appl. Surf. Sci.*, 2018, **439**, 605.
45 A. Priebe, T. Xie, G. Bürki, L. Pethö and J. Michler, The matrix effect in TOF-SIMS analysis of two-element inorganic thin films, *J. Anal. At. Spectrom.*, 2020, **35**, 1156.
46 Z. Zhang, D. Zhang, L. Lyu, G. Cui and H. Lu, In situ formation of Z-scheme Bi_2WO_6/WO_3 heterojunctions for gas-phase CO_2 photoreduction with H_2O by photohydrothermal treatment, *Catalysts*, 2022, **12**, 1237.
47 A. Marikutsa, L. Yang, A. N. Kuznetsov, M. Rumyantseva and A. Gaskov, Effect of W–O bonding on gas sensitivity of nanocrystalline Bi_2WO_6 and WO_3, *J. Alloys Compd.*, 2021, **856**, 158159.
48 Y. Huang, S. Kou, X. Zhang, L. Wang, P. Lu and D. Zhang, Facile fabrication of Z-scheme Bi_2WO_6/WO_3 composites for efficient photodegradation of bisphenol A with peroxymonosulfate activation, *Nanomaterials*, 2020, **10**, 724.
49 J. Zhang, P. Deng, M. Deng, H. Shen, Z. Feng and H. Li, Hybrid density functional theory study of native defects and nonmetal (C, N, S, and P) doping in a Bi_2WO_6 photocatalyst, *ACS Omega*, 2020, **5**, 29275.
50 W. Shockley, The theory of p–n junctions in semiconductors and p–n junction transistors, *Bell Syst. Tech. J.*, 1949, **28**, 435.
51 S. Dushman, Thermionic emission, *Rev. Mod. Phys.*, 1930, **2**, 381.
52 Y. Yao, R. Gangireddy, J. Kim, K. K. Das, R. F. Davis and L. M. Porter, Electrical behavior of β-Ga2O3 Schottky diodes with different Schottky metals, *J. Vac. Sci. Technol., B*, 2017, **35**, 03D113.
53 L. A. M. Lyle, K. Jiang, E. V. Favela, K. Das, A. Popp, Z. Galazka, G. Wagner and L. M. Porter, Effect of metal contacts on (100) β-Ga_2O_3 Schottky barriers, *J. Vac. Sci. Technol., A*, 2021, **39**, 033202.
54 X. Long, W. Niu, L. Wan, X. Chen, H. Cui, Q. Sai, C. Xia, D. N. Talwar and Z. Feng, Optical and Electronic Energy Band Properties of Nb-Doped β-Ga_2O_3 Crystals, *Crystals*, 2021, **11**, 135.
55 R. Seino, H. Asai, I. Takakuwa, S. Asanuma, Y. Nemoto, Y. Nishimiya, K. Nishio and M. Minohara, Design of oxide-based tunnel FETs using amorphous IGZO and p-type oxide semiconductors, *J. Appl. Phys.*, 2025, **138**, 105306.
56 L.-L. Yang, Y.-S. Peng, Z. Liu, M.-L. Zhang, Y.-F. Guo, Y. Yang and W.-H. Yang, *Chin. Phys. B*, 2023, **32**, 047301.